Bulletin of the Seismological Society of America, Vol. 102, No. 4, pp. 1348–1360, August 2012, doi: 10.1785/0120110201

Source Characterization of Near-Surface Chemical Explosions at SAFOD

by Fred F. Pollitz, Justin Rubinstein, and William Ellsworth

Abstract A series of near-surface chemical explosions conducted at the San Andreas Fault Observatory at Depth (SAFOD) main hole were recorded by high-frequency downhole receiver arrays in April 2005. These seismic recordings at depths ranging from the surface to 2.3 km constrain the shallow velocity and attenuation structure as well as the first-order characteristics of the source. Forward modeling of the explosions indicates that a source consisting of combined explosion, delayed implosion, and second-order moment-tensor components (corresponding to a distribution of vertical shear dislocations in the rock directly above the explosion) is sufficient to characterize the generated seismic wave fields to first order. Grid searches over source parameters controlling the nonexplosive components allow for the quantification of distributed vertical shear above the source and the estimation of the moment and time delay of the implosive component relative to the explosion. An estimated implosive to explosive moment ratio of 0.34 to 0.43 indicates a net static moment and positive macroscopic volume change.

Introduction

The crust surrounding the San Andreas Fault Observatory at Depth (SAFOD) has been the focus of a comprehensive and coordinated group of crustal structure investigations as part of the National Science Foundation's EarthScope program (Zoback *et al.*, 2010). The SAFOD main hole is a deviated well extending to about 2.5-km depth that has allowed geological sampling and geophysical monitoring of recurrent seismicity along the active San Andreas fault, which is about 2 km to its northeast. As part of the geophysical modeling associated with the SAFOD main hole, test shots were conducted in April 2005 by the U.S. Geological Survey (USGS) into the borehole array contributed by Paulsson Geophysical Services, Inc. (PGSI; Fig. 1). The generated seismic wave fields were recorded by the PGSI downhole receiver array consisting of 80 high-frequency three-component geophones with a station spacing of 15.24 m. Deployed at three levels, the array covered the depth range from the surface to 2.3 km. The original purpose of these shots was to calibrate these seismic instruments for use in passive recording of local seismic events as well as to independently characterize the layered velocity structure, complementing detailed geologic, and geophysical logs (e.g., Chavarria *et al.*, 2003, 2007; McPhee *et al.*, 2004).

The PGSI shot recordings have proven to be very useful for understanding the nature of high-frequency seismic wave propagation in the near field. Although an underground explosion is expected to be an isotropic source and to generate primarily *P* waves, *S* waves are commonly observed in far-field seismic recordings of contained chemical explosions and underground nuclear explosions, and nonisotropic source components are inferred (Dreger and Woods, 2002). Prevailing hypotheses of *S*-wave generation include tectonic strain relaxation (Press and Archambeau, 1962; Toksöz *et al.*, 1965), *P*- to *S*-wave scattering (Woods and Helmberger, 1997), and the effect of interaction with the free surface including spall, cracking, and nonlinear deformation (Stevens *et al.*, 1991; Patton and Taylor, 1995, 2011). The objective of this study is to characterize the source in sufficient detail to identify possibly nonexplosive source components, shedding light on the conversion of *P*-wave to *S*-wave energy in the near field as the radiated wave field leaves the source and interacts with the medium.

Data Set

Six shots at a depth of ~3 m were detonated adjacent to the SAFOD main hole on 28–29 April and 6 May 2005. They were recorded by omnidirectional SMC-1850 geophones with a natural frequency of 15 Hz and a damping constant of 0.47, arranged in 80 three-component sections. We focus on three shots that sample three different (and overlapping) levels of PGSI-array deployment and are labeled as follows: shot 2, shallow array from 0.05 to 1.25 km; shot 3, intermediate array from 0.93 to 2.00 km; and shot 5, deep array from 1.54 to 2.36 km (Table 1). Although three-component velocity has been recorded for these shots, only the axial component (i.e., the component parallel to the local inclination of the borehole) is unambiguously oriented for all three shots. Therefore, we focus on this single-velocity component for most quantitative comparisons (cross borehole components will be considered briefly in the Discussion section).

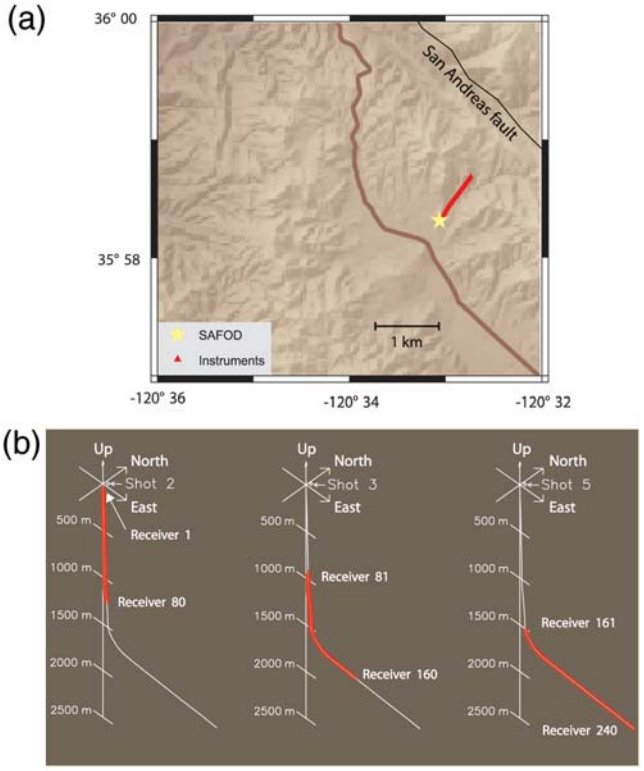

Figure 1. Location of the PGSI receiver array in (a) map view and (b) depth view. The three shots used in this study are located within 30 ft of one another on the surface and are indistinguishable in this map view.

For each of the three shots described in Table 1, Figure 2 shows record sections of axial velocity. (See the Data and Resources section.) Figure 3 shows a subset of these records displayed as seismograms for every tenth downhole receiver, as well as the shallowest eight receivers that recorded shot 2. Each record section illustrates a prominent *P*-wave arrival and additional coherent arrivals that may represent a combination of more complicated downgoing waves (e.g., *P*-wave reverberations from near-surface structure), upgoing or horizontal waves generated by reflections from relatively deep sharp discontinuities or the nearby San Andreas fault (e.g., fig. 6 of Chavarria *et al.*, 2007), and possibly *S* waves. It is noteworthy that *S* waves are only observed on the shallowest recordings (i.e., shot 2) and likely originate from *P*–*S* conversions at lithologic boundaries. The lack of a discernible surface-converted *S* wave (i.e., *pS* phase) for shot 2 places constraints on its source mechanism. Waveforms after direct *P* for shots 3 and 5 are more complicated than expected for a purely explosive source and demand secondary source components. In order to guide our interpretation of the recorded wave field at depth, we employ wave field modeling and compare synthetic seismograms with the available recordings.

Methods

Synthetic seismograms are generated using the direct Green's function (DGF) method of Friederich and Dalkolmo (1995). This method synthesizes the seismic wave field for a spherically layered structure of seismic velocities V_P and V_S, density ρ, and attenuation factors Q_P and Q_S in the $l-\omega$ domain, where l denotes the spherical harmonic degree. It is the spherical equivalent of the frequency–wavenumber (*f-k*) method employed for flat-layered structures (e.g., Zhu and Rivera, 2002). It was coded by the first author of this paper and validated against analytic solutions, including those for elastic wave propagation in a full space for both isotropic and shear sources (equation 4.29 of Aki and Richards, 1980) and in a half-space, for example, Lamb's problem (Kuhn, 1985), as well as the independent numerical solutions AXITRA (Bouchon, 1981) and the *f-k* method (Zhu and Rivera, 2002).

The DGF method is applied to buried sources in the layered structure given in Figure 4. The V_P structure in this figure is determined by the *P* arrival times of the shots (Fig. 3), the V_S structure is based on the V_P structure and the V_P/V_S ratio determined by regional tomography (Zhang *et al.*, 2009), and the density structure is based on empirical $V_P-\rho$ relationships (Gardner *et al.*, 1974; Brocher, 2005). Specifically, we use the V_P/V_S ratio in the vicinity of $(X,Y)=(0,0)$ in figure 5 of Zhang *et al.* (2009), which is everywhere between 1.8 and 2.0, somewhat higher than indicated by well log data (fig. 8 of Zhang *et al.*, 2009); we use the Gardner *et al.* (1974) curve in figure 1 of Brocher (2005) to specify the density. The Q_P structure is based on fitting the decay in *P*-wave amplitude as a function of downhole distance using forward waveform modeling; it is consistent with modeling the *P*-wave pulse width as a function of propagation distance (Rubinstein *et al.*, 2011). The Q_S values are not estimated from the data but are chosen such that the quality factor for bulk modulus is twice that of shear modulus.

For an *x*–*y*–*z* coordinate system (where *x*, *y*, and *z* denote distances in the east, north, and up directions, respectively) and a point source located at $\mathbf{r}_0=(x_0,y_0,z_0)$, we consider a moment-tensor density $\mathbf{M}(\mathbf{r})$ given by

$$\begin{aligned}\mathbf{M} = {} & M_{\text{expl}}\begin{bmatrix}1&0&0\\0&1&0\\0&0&1\end{bmatrix}H(t)\delta(\mathbf{r},\mathbf{r}_0)\\ & -M_{\text{impl}}\begin{bmatrix}1&0&0\\0&1&0\\0&0&1\end{bmatrix}H(t-\delta t_{\text{impl}})\delta(\mathbf{r},\mathbf{r}_0)\\ & -M_{xxz}\begin{bmatrix}0&0&1\\0&0&0\\1&0&0\end{bmatrix}H(t)\partial_{x_0}\delta[\mathbf{r},(x_0,y_0,z')]\\ & -M_{yyz}\begin{bmatrix}0&0&0\\0&0&1\\0&1&0\end{bmatrix}H(t)\partial_{y_0}\delta[\mathbf{r},(x_0,y_0,z')],\end{aligned} \tag{1}$$

Table 1
Details of Small-Offset Shots from SAFOD Wellhead

Shot Number	Date (mm/dd/yy)	Time, UTC (hh:mm:ss.ssssss)	Number of holes (Depth, 10 ft)	Shot Size (lb)	Northing Offset (ft)	Easting Offset (ft)
2	04/28/05	21:25:00.000197	1	7	97.5	89.1
3	04/29/05	15:05:00.000124	2 (@ 5 lbs)	10	112.0	65.4
5	04/29/05	20:28:00.000043	2 (@ 5 lbs)	10	103.9	77.7

where $H(t)$ is the step function, $\delta(\mathbf{r}, \mathbf{r}_0)$ is the Dirac delta function, M_{expl} and M_{impl} are the moments associated with explosion and implosion source components, respectively, δt_{impl} is the delay in the implosive component, and M_{xxz} and M_{yyz} represent second-order moment-tensor components (Backus and Mulcahy, 1976) that we shall relate to a

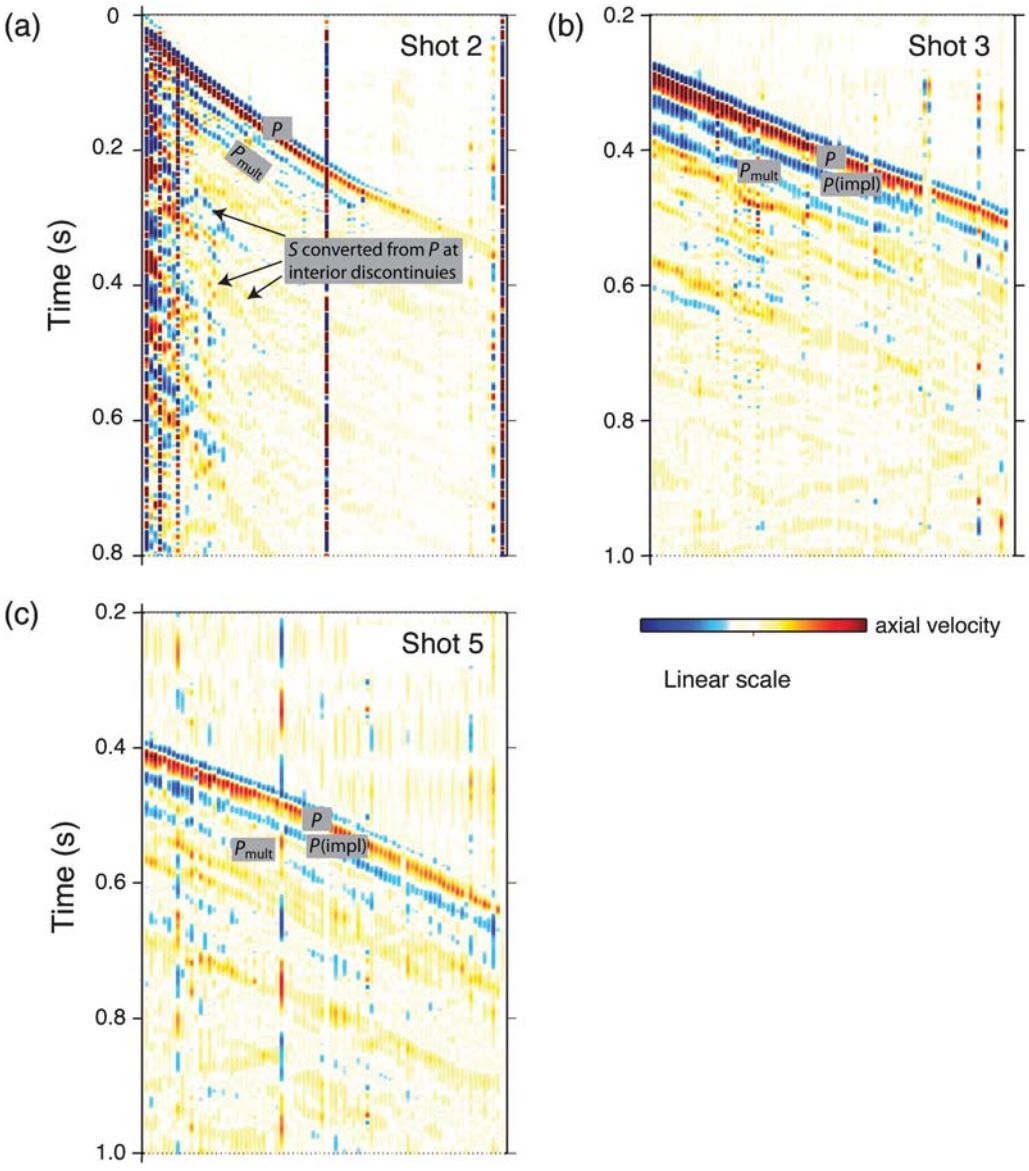

Figure 2. Record sections of PGSI axial-component recordings for (a) shot 2, (b) shot 3, and (c) shot 5 (Table 1). Each is a composite of 80 seismograms displayed in order of increasing depth within each section. Observed traces have been deconvolved to velocity using an acausal filter generated by a cosine taper in the frequency domain between $\omega_c = 2\pi/T_c$ and $2\omega_c$, where T_c is a corner period chosen to be 0.023 s; the corresponding corner frequency is $\omega_c/2\pi = 43.5$ Hz. Each seismogram is scaled up with a gain factor proportional to the square root of receiver depth. Selected seismic phases are indicated. P(impl) denotes implosion-generated P (see the Nonexplosive Source Components section).

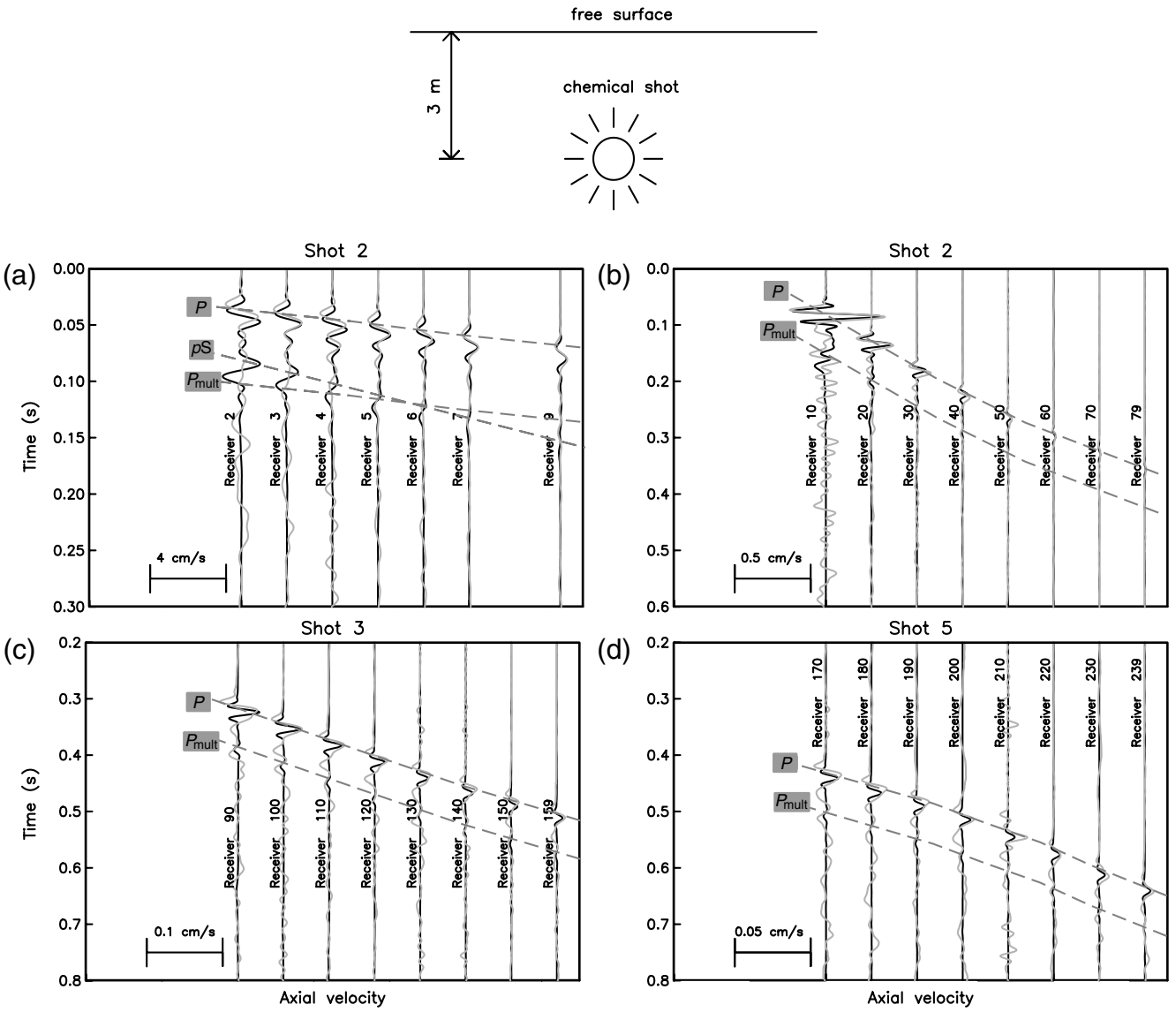

Figure 3. Observed axial-component seismograms (gray) and synthetic seismograms (black) for each of the three shots recorded by downhole receiver arrays (Table 1). Parts (a)–(d) show different shots and/or groups of receivers. Both observed and synthetic traces have been deconvolved to velocity as described in Figure 2. All traces are true amplitude, that is, identical scaling of individual traces for each shot. Only the explosion component M_{expl} is used to generate these synthetics; other source components of equation (1), that is, M_{impl}, M_{xxz}, and M_{yyz}, are zero. Selected seismic phases are shown by dashed gray lines.

distribution of vertical shear in a volume above $\mathbf{r}_0$. The notation (x_0, y_0, z') for these components is used to emphasize the fact that the effective point source may be taken at a depth z' different from that of the explosive component z_0. The representations of M_{xxz} and M_{yyz} in equation (1) may be verified by evaluating equation 5.1b of Backus and Mulcahy (1976). This involves multiplying equation (1) by $(x_0 - x)$ or $(y_0 - y)$, integrating over a volume $dV = dx_0 dy_0 dz'$, and integrating by parts with respect to x_0 (for M_{xxz}) or y_0 (for M_{yyz}).

Although it does not play a prominent role in the interpretations of the recordings considered in this paper, for a special case (i.e., a subset of shot 2 recordings) we shall consider a representation of the source in terms of first-order moment-tensor components:

$$\mathbf{M} = M_{\text{expl}} \begin{bmatrix} 1 & 0 & 0 \\ 0 & 1 & 0 \\ 0 & 0 & 1 \end{bmatrix} H(t)\delta(\mathbf{r}, \mathbf{r}_0) + \begin{bmatrix} 0 & M_{xy} & M_{xz} \\ M_{xy} & 0 & M_{yz} \\ M_{xz} & M_{yz} & 0 \end{bmatrix} H(t)\delta(\mathbf{r}, \mathbf{r}_0). \quad (2)$$

The second term corresponds to a combination of shear dislocations.

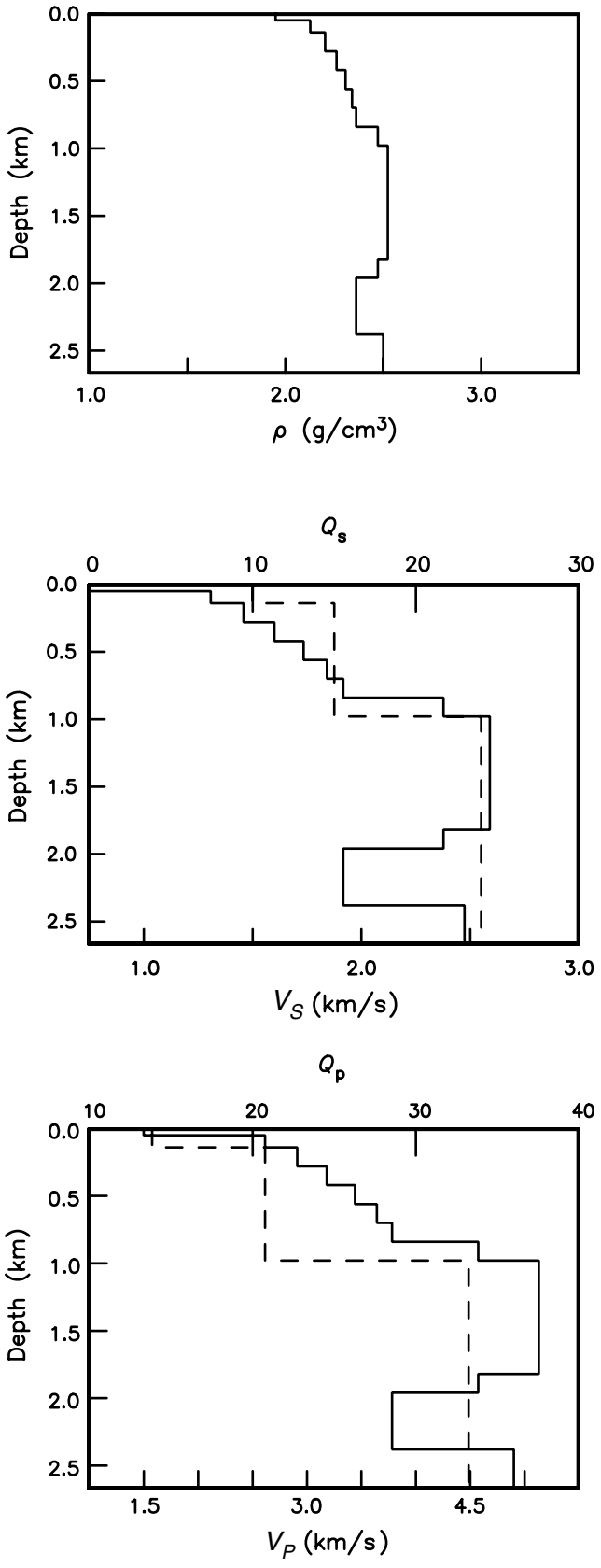

Figure 4. Layered structure of P and S velocities V_P and V_S, respectively, density ρ, and P- and S-wave quality factors Q_P and Q_S (dashed lines), respectively, as a function of depth.

The representations in equations (1) and (2) shall be evaluated separately; that is, second-order moment-tensor components shall not be mixed with shear dislocations in any of the models considered.

Explosive Source

Synthetic seismograms using an explosive source and corresponding to the various shots are shown by the black traces in Figure 3. For shot 2, the explosive source moment used for the synthetics is $M_{\text{expl}} = 1.1 \times 10^{10}$ N · m, and for shots 3 and 5 it is $M_{\text{expl}} = 4.3 \times 10^{10}$ N · m. These values were chosen to match the amplitude of the P waveforms. The inclination of the borehole is within 5° of vertical for the first 1700 m and is progressively steeper as the depth increases, up to 55° at 2.3 km depth with a dip toward the northeast. Thus, the axial-component velocity is dominated by the vertical velocity in the upper 1500 m and includes a progressively larger northeastward component as the depth increases. The theoretical seismic radiation field depends upon the shot and receiver depths and the horizontal offset between shots and receivers. These horizontal offsets are generally less than 50 m in the upper 1500 m but increase at greater depth up to about 850 m at 2.3 km.

In order to guide the interpretation of observed and synthetic record sections in the vertical direction, we construct record sections in the horizontal direction at the depths of receivers 30 and 60 (Fig. 5a and Fig. 5b, respectively). Prominent arrivals include direct P and pS but also multiple reflections between the free surface and the base of a low-velocity near-surface layer. It is noteworthy that a nonzero pS arrival is present even at zero offset, the amplitude of pS generally grows with horizontal offset, and the zero-offset pS amplitude diminishes rapidly with depth; these results also obtained by Kuhn (1985). P travel times from the shallowest receivers indicate a steep velocity gradient in the upper 100 m, with V_P increasing from ~1.5 km/s at the surface to 2.6 km/s at 100 m. This is represented by two layers in the upper 100 m (Fig. 4), with the uppermost 50 m being of very low velocity (Fig. 5 inset). Because the model discontinuity at 50 m is very sharp, P-wave reverberations are generated between the surface and this depth. The reverberations generated between the surface and this depth are labeled as P_{mult}. The two-way travel time is 100 m/(1.5 km/s) = 0.067 s. This is the difference in travel time between the direct P wave and successive reverberations that follow it (Fig. 5).

Figure 6 shows the synthetic record sections of the three shots using only explosive source components. Comparison with the observed record sections of Figure 2 reveals that the P and P_{mult} phases are generally replicated in the synthetics, but first-order differences remain. For shot 2, the synthetics predict a prominent pS phase on the shallowest receivers, which is not observed. For shots 3 and 5, the observed waveforms following direct P are more complicated than those predicted by the explosive-source model. These comparisons

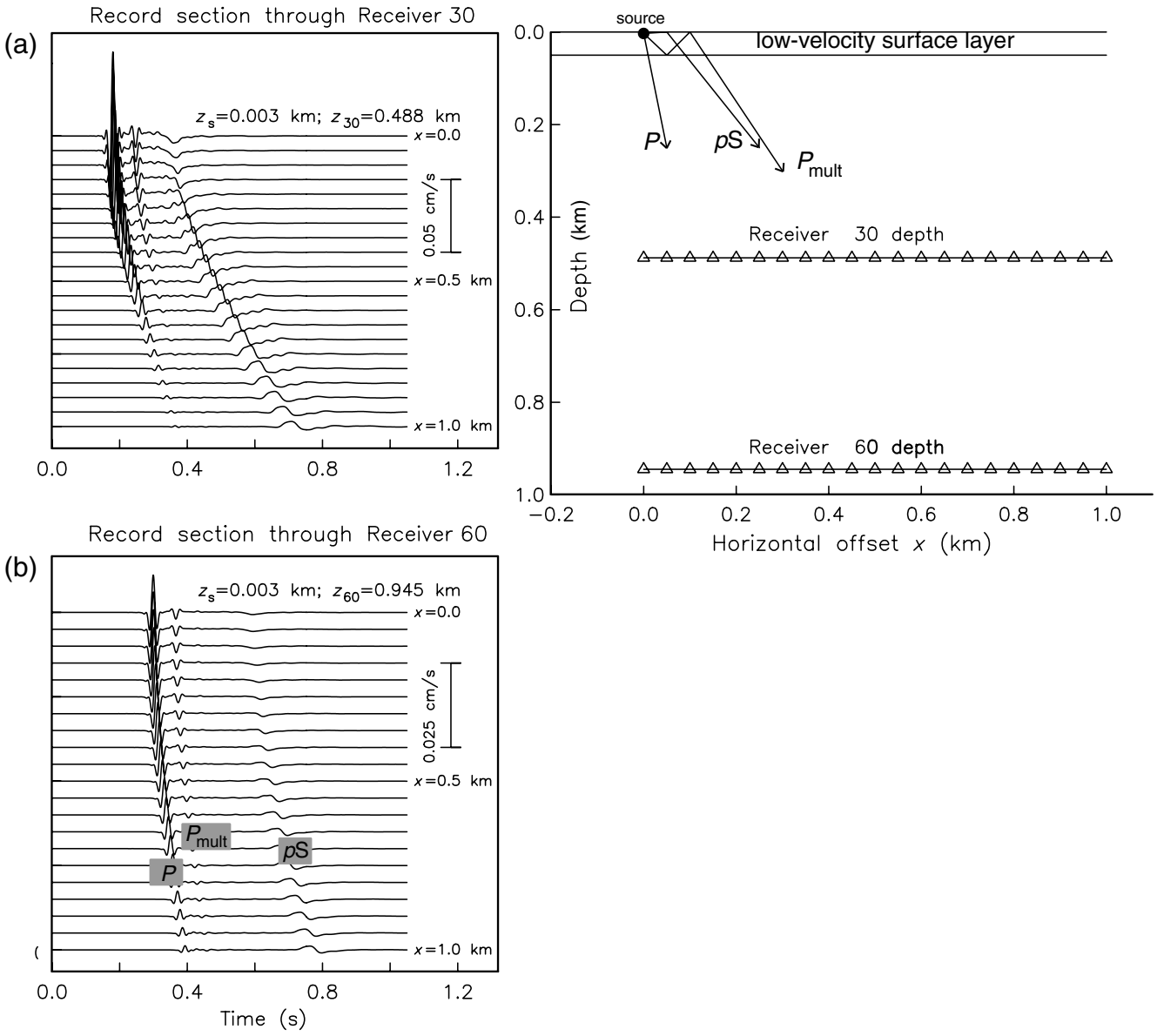

Figure 5. Vertical-component velocity seismograms as a function of lateral distance x from an isotropic source buried 3 m deep. (a) Fictitious array at the depth of receiver 30 (0.4884 km). (b) Fictitious array at the depth of receiver 60 (0.9455 km). The inset indicates the geometry of direct P, pS, and multiple reflections between the free surface and the base of the low-velocity near-surface layer P_{mult}. The observed receiver 30 and 60 traces in Figure 3b are most comparable to the $x = 0$ synthetics.

point to the need for nonexplosive source components to explain the observed waveforms.

Nonexplosive Source Components

Inference of nonexplosive source components is based on a grid search for optimal values of the source parameters (some subset of M_{impl} plus δt_{impl}, M_{xxz}, and M_{yyz}, corresponding to the second, third, and fourth terms of equation 1) in which the root-mean-square (rms) misfit between the observed and synthetic waveforms is minimized. For this purpose, a time window of length 0.15 s starting just before the P arrival is used to calculate the squared misfit, which is then summed over all contributing records and averaged. The secondary source components are assumed to be impulsive.

Figure 3 includes the theoretical P, pS, and P_{mult} arrivals determined by the synthetics with only the explosive source component. In Figures 2 and 3, both direct P and P_{mult} are unambiguously observed at all depths below that of receiver 10 (depth = 183 m) for shot 2, and they are replicated by the synthetics. In the shallowest shot 2 recordings (Fig. 3a), neither pS nor P_{mult} is clearly identified because of the interference between them and with the secondary source components.

In records 2–3 for shot 2 (Fig. 3a), the most prominent arrival in the synthetic seismograms is pS, which

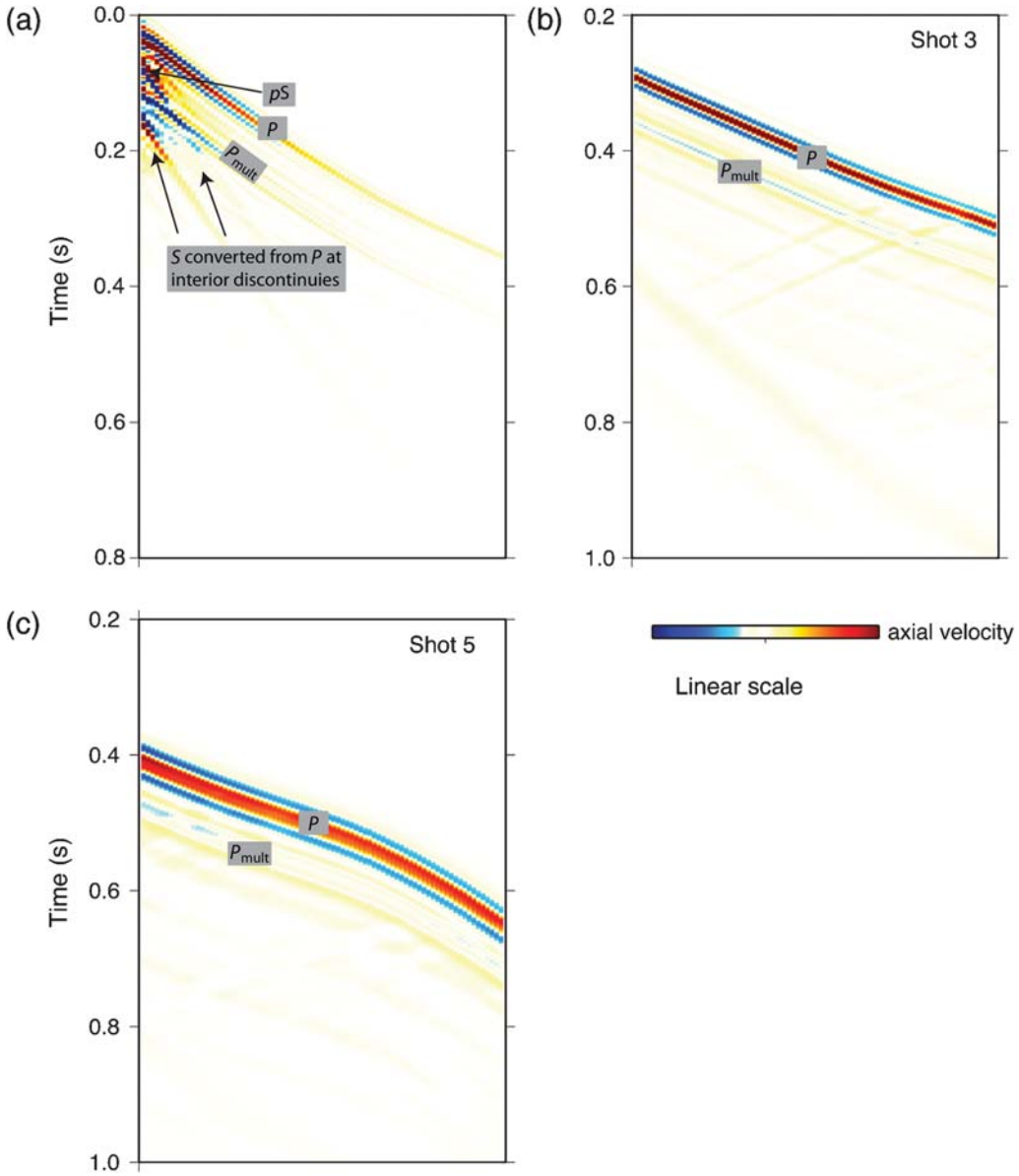

Figure 6. Synthetic record sections of PGSI axial-component recordings for (a) shot 2, (b) shot 3, and (c) shot 5 (Table 1). Each is a composite of 80 seismograms displayed in order of increasing depth within each section. For each shot, the source is purely explosive. Synthetic traces have been deconvolved to velocity as described in Figure 2. Each seismogram is scaled up with a gain factor proportional to the square root of receiver depth. Selected seismic phases are shown.

follows direct P by about 0.06 s; its relatively large amplitude is due to the horizontal shot-receiver offset of ~40 m, which is a large fraction of the receiver depth (61.9 and 77.1 m for records 2–3). The lack of such an arrival in the observed seismograms is an important clue to the source process. The addition of an implosion source (e.g., the M_{impl} term in equation 1) with modest delays δt_{impl} modifies synthetic waveforms only in the time interval between P and pS. Possible P-wave arrivals arising from a strong implosive component, as seen by the arrivals designated P_{impl} in Figure 2b and Figure 2c for shots 3 and 5, respectively, are not seen for shot 2 (Fig. 2a), and the introduction of an implosive component in trial runs does not improve the fit to shot 2 waveforms. Possible secondary source components that could augment the isotropic moment-tensor components include point sources of shear (including compensated linear vector dipole [CLVD] components) and distributed shear.

We find that a model of distributed secondary vertical shear, on vertical planes close to the source depth, best replicates the observed seismograms. Our preferred model involves a distribution of vertical shear on vertical planes that comprise a cylinder of diameter Δx, laterally centered on the position of shot 2 and placed at a nominal depth of 1.5 m. The moment-tensor density components on the cylinder are of the form $M_{nz} = \text{constant} = -M'$, where n denotes the direction perpendicular to the surface of the cylinder

toward its exterior. The secondary shear dislocations are collapsed onto the cylinder surface at depth 1.5 km so that they are distributed over a circle of circumference $C = \pi\Delta x$. Because Δx is small, it can be shown that this distribution is equivalent to the superposition of two second-order moment-tensor components (Backus and Mulcahy, 1976) given by

$$M_{xxz} = M_{yyz} = -\frac{1}{4}(M'C)\Delta x. \quad (3)$$

We calculate the corresponding synthetics using the first, third, and fourth source terms of equation (1), which for fixed M_{expl} depend upon M_{xxz} and M_{yyz}, which are equal according to equation (3). A grid search for optimal M_{xxz} is done using receivers 2–7 and 9 of shot 2. This results in the values $M_{xxz} = M_{yyz} = -(1.72\text{ m}) \times M_{\text{expl}}$ (Fig. 7), where $M_{\text{expl}} = 1.1 \times 10^{10}$ N · m for shot 2 (Explosive Source section). The resulting superposition of the isotropic moment tensor and higher-order moment-tensor components for the shallow recordings of shot 2 are shown in Figure 8. This model of a combined isotropic first-order moment tensor and shear-type second-order moment tensor reduces the amount of shear-wave energy arising from the near surface; that is, the explosion-generated *pS* and secondary *S*, labeled as *pS* + *S* (secondary) in Figure 8a, destructively interfere. This model fits the shallowest shot 2 recordings better than the model of isotropic source alone (Fig. 3). The fits to recordings at greater depth (e.g., shot 2 seismograms at the depth of receiver 10 and greater shown in Fig. 8b) are found to be negligibly changed by the addition of the second-order moment-tensor components.

For shots 3 and 5, energy arriving 0.02–0.03 s after direct *P* and of opposite polarity is best explained as the result of an implosive source acting with a small time delay after the initial chemical shot. We calculate the corresponding synthetics using the first and second source terms of equation (1), with M_{impl} and δt_{impl} determined through a grid search. For shot 3,

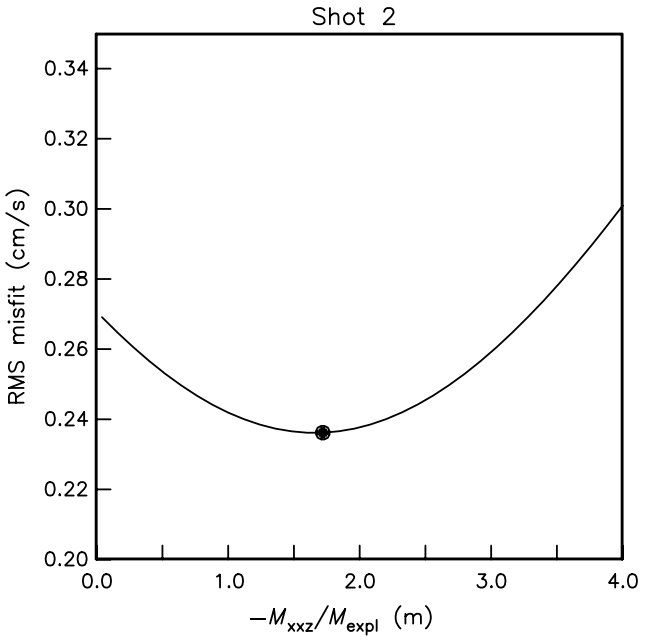

Figure 7. Root-mean-square misfit between the observed and synthetic seismograms for shot 2 computed using 0.15 s-long portions of the contributing seismograms beginning just before the *P* arrival. The synthetics are calculated using the first, third, and fourth source terms of equation (1); the third and fourth terms are parameterized with second-order moment-tensor components M_{xxz} and M_{yyz}, which are equal (equation 3). The optimal $M_{xxz} = M_{yyz} = -(1.72\text{ m}) \times M_{\text{expl}}$ is shown by the solid circle.

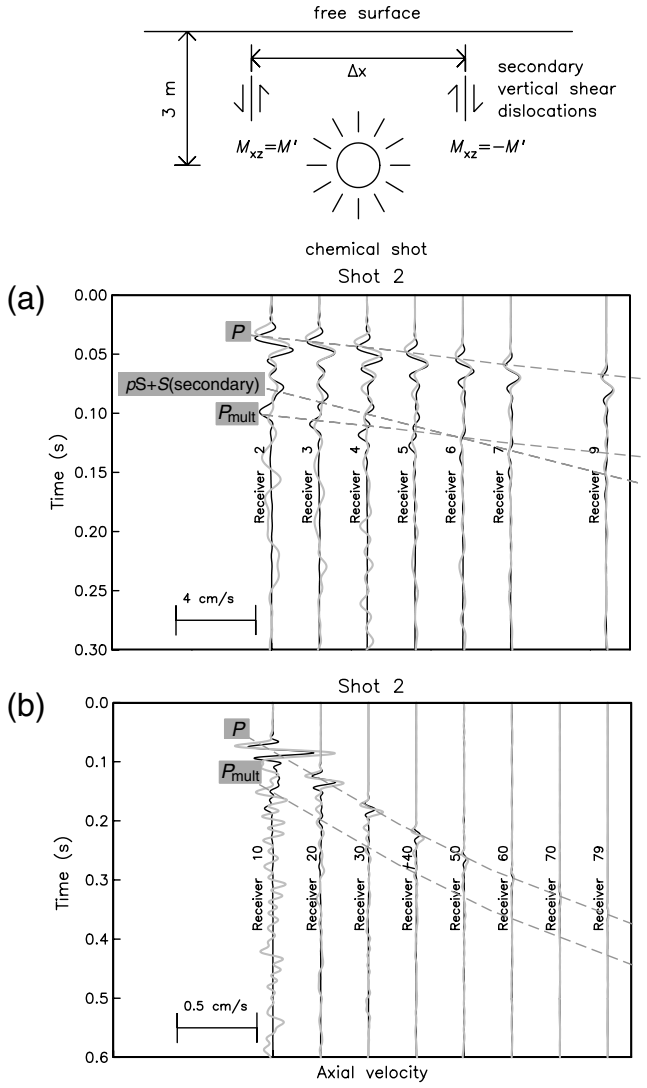

Figure 8. Observed axial-component seismograms (gray) and synthetic seismograms (black) for shot 2 (Table 1). Parts (a) and (b) show shot 2 results for different groups of receivers. Synthetics are calculated using the combined explosion source and higher-order moment-tensor model (see Nonexplosive Source Components section). The inset indicates the geometry of the moment-tensor density on the edge of a cylinder of diameter Δx used to represent secondary shear dislocations. Selected seismic phases are shown by dashed gray lines. The designation *pS* + *S*(secondary) denotes the combination of explosion-generated *pS* and secondary *S*. Other details are as in Figure 3.

receivers 90, 100, 110, 120, 130, 140, 150, and 159 are used; for shot 5, receivers 170, 180, 190, 200, 210, 220, 230, and 239 are used. This analysis yields optimal $M_{\rm impl} = 0.43\times M_{\rm expl}$ and $\delta t_{\rm impl} = 0.027$ s for shot 3 (Fig. 9a), and $M_{\rm impl} = 0.34 \times M_{\rm expl}$ and $\delta t_{\rm impl} = 0.027$ s for shot 5 (Fig. 9b). The resulting synthetics are shown in Figure 10a,b. The implosion-generated *P*, labeled as *P*(impl) in Figure 10a for shot 3, partially interferes with the explosion-generated *P*, labeled as *P*. The improvement in the fit over the corresponding synthetics for a purely isotropic source (Fig. 3c,d) comes mainly from the M_{zz} component of the implosive source. Because of the high attenuation of *S* waves down to depth $\gtrsim 1$ km from near-surface sources, shot 3 and 5 synthetics are nearly insensitive to possible CLVD components in either the explosive or implosive parts of the source.

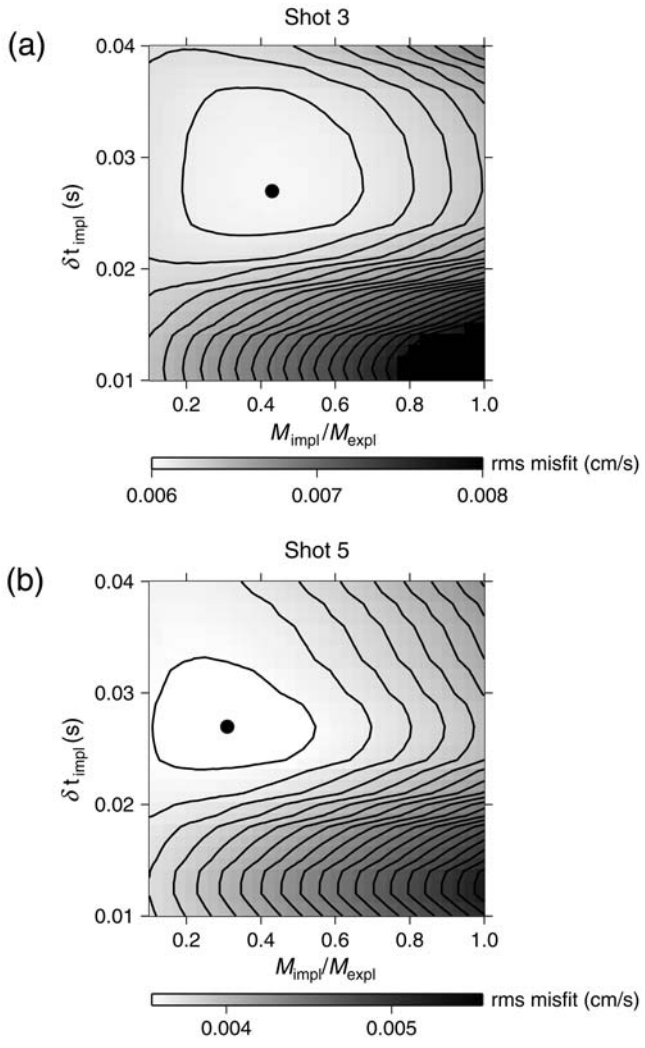

Figure 9. Root-mean-square misfit between observed and synthetic seismograms computed using 0.15 s-long portions of the contributing seismograms beginning just before the *P* arrival. The synthetics are calculated using the first two source terms of equation (1); the second term is parameterized with implosive moment $M_{\rm impl}$ and time delay $\delta t_{\rm impl}$. (a) Shot 3, with optimal $M_{\rm impl} = 0.43 \times M_{\rm expl}$ and $\delta t_{\rm impl} = 0.027$ s (solid circle). (b) Shot 5, with optimal $M_{\rm impl} = 0.34 \times M_{\rm expl}$ and $\delta t_{\rm impl} = 0.027$ s (solid circle).

Discussion

Figure 11 shows synthetic record sections of the three shots using the various optimized secondary source components. These may be directly compared with the observed record sections in Figure 2. For all shots, the synthetic *P* and $P_{\rm mult}$ phases generally match the corresponding phases in the observed record sections (Fig. 2). The addition of the higher-order moment-tensor components for shot 2 produces an additional *S* arrival that destructively interferes with the *pS* arrival generated by the explosive source component. The combination is labeled as $pS + S$(secondary) in Figure 11a. (Comparison between observed and synthetic waveforms for shot 2 is best seen in Fig. 8.) The delayed implosion

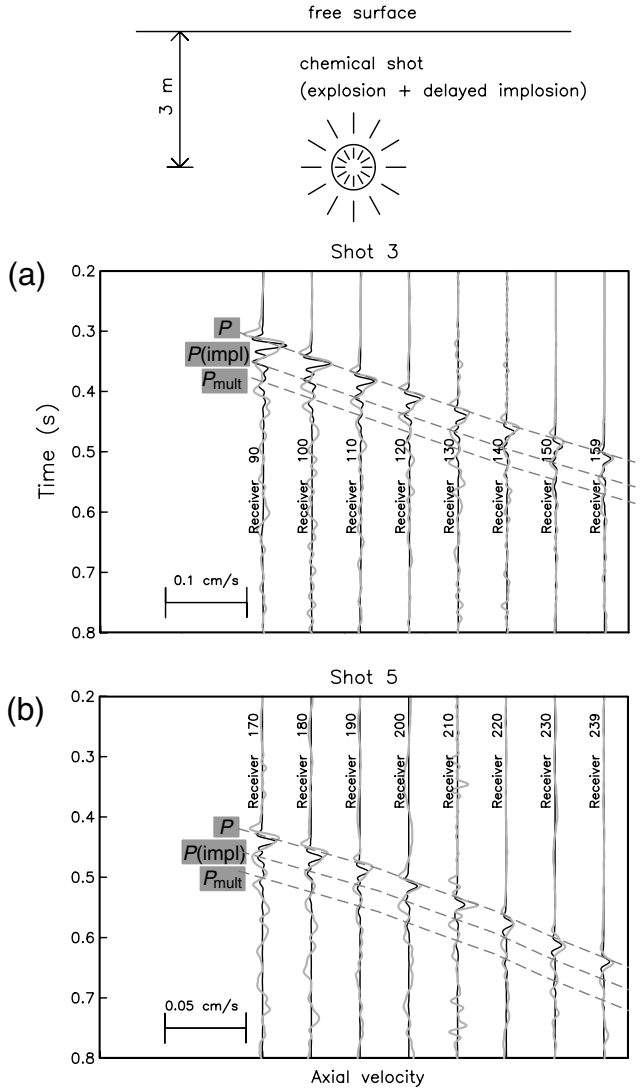

Figure 10. Observed axial-component seismograms (gray) and synthetic seismograms (black) for (a) shot 3 and (b) shot 5 (Table 1). For shots 3 and 5, the synthetics are calculated using the combined explosion source and delayed implosion model (see Nonexplosive Source Components section). Selected seismic phases are indicated with dashed gray lines. The designation *P*(impl) denotes the implosion-generated *P*. Other details are as in Figure 3.

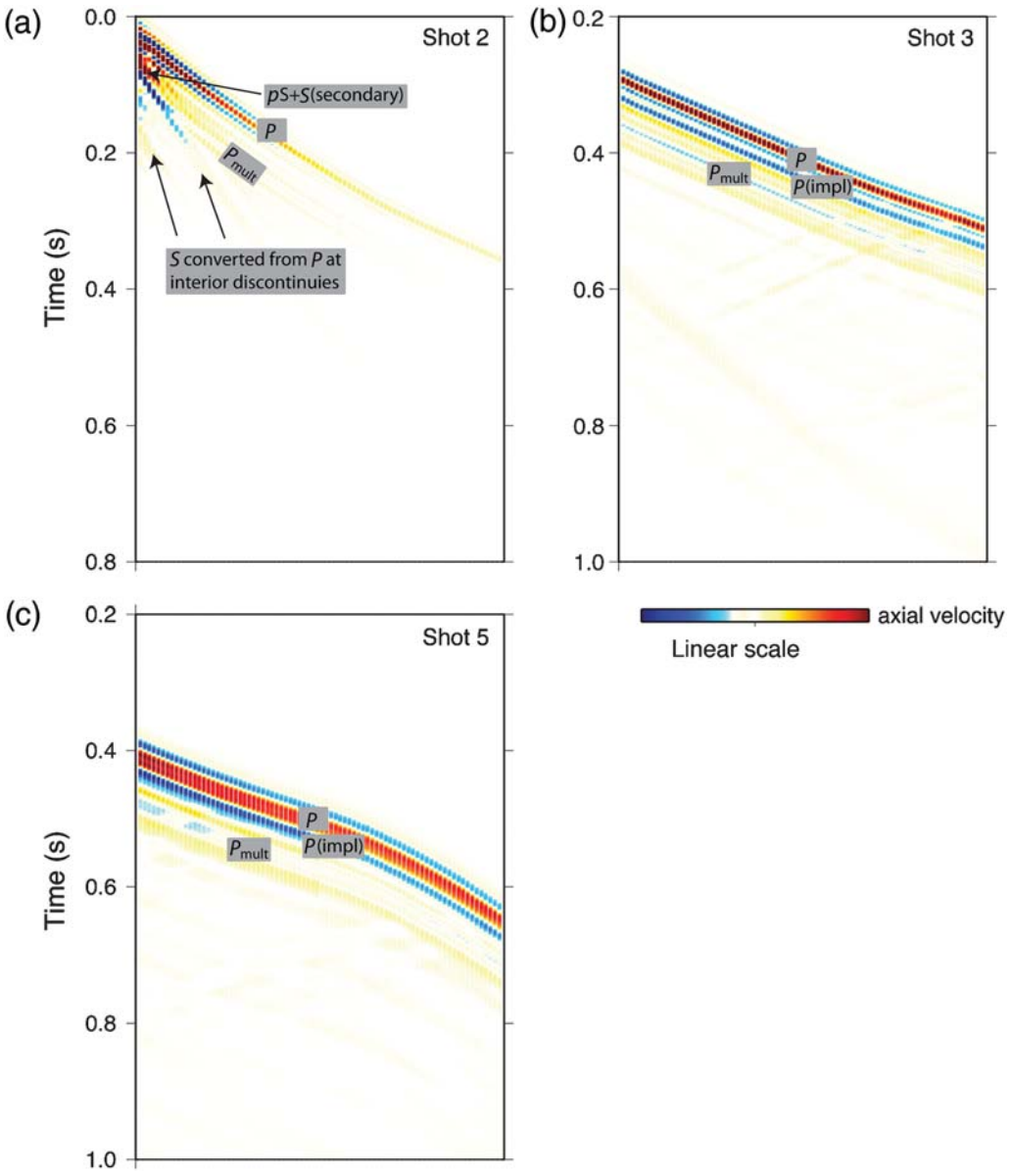

Figure 11. Synthetic record sections of PGSI axial-component recordings for (a) shot 2, (b) shot 3, and (c) shot 5 (Table 1). Each is a composite of 80 seismograms displayed in order of increasing depth within each section. For each shot, the source is a combination of an explosion plus a secondary source component as presented in the Nonexplosive Source Components section. Synthetic traces have been deconvolved to velocity as described in Figure 2. Each seismogram is scaled up with a gain factor proportional to the square root of receiver depth. Selected seismic phases are indicated. *P*(impl) denotes the implosion-generated *P*. $pS + S$(secondary) denotes the combination of the explosion-generated pS and M_{xxz}- and M_{yyz}-generated S.

sources implemented for shots 3 and 5 produce waveforms (Fig. 11b,c) that qualitatively explain the large negative axial-component arrival following direct *P* (Fig. 2b,c) as well as the waveforms over the subsequent 0.05–0.1 s, that is, the P_{mult} phase, which we interpret to be composed of contributions from the explosive and nonexplosive source components.

Trials of alternative models aimed at explaining, in particular, the character of the shallow shot 2 recordings in Figure 3a were conducted using additional shear components of a first-order moment tensor, that is, equation (2). These trials indicate that models involving the addition of a point vertical shear dislocation on any vertical plane (i.e., a nonzero M_{xz} or M_{yz} component in addition to the M_{expl} component) fail to explain the absence of energy traveling with the S wavespeed in the shot 2 recordings.

A stronger alternative model to explain the shallow shot 2 recordings involves horizontal shear on a vertical plane, that is, an M_{xy} component in addition to the M_{expl} component of the chemical shot (equation 2). A grid search for optimal M_{xy} yields $M_{xy} = 0.20 \times M_{\text{expl}}$ (Fig. 12); the resulting misfit is smaller than that obtained for the second-order moment-tensor model (Fig. 7). This model fits the observed seismograms remarkably well (Fig. 13). It would require strong horizontal shear stresses to be generated by the

chemical explosion, causing failure of the surrounding rock. It would be plausible if there were strong asymmetry in the M_{xx} and M_{yy} components of the chemical shot, leading to strong horizontal shear at the source depth, or if lateral variations in material properties led to a similar concentration of horizontal shear. Hole-transverse component seismograms provide an additional means of comparing the second-order moment-tensor and horizontal shear models of secondary sources. Figure 14 shows sets of observed and model seismograms for these two models. The amplitude of motion transverse to the borehole (which is practically horizontal for the shallowest recordings of shot 2), determined from the three-component seismograms, is the plotted quantity; phase information is not available because the nonaxial recorded components are of uncertain orientation. The horizontal shear model (Fig. 14b) exhibits more energy traveling at the S wavespeed (arriving at ≈0.09 and 0.10 s for receivers 2 and 3, respectively) than the second-order moment-tensor model. Although the observed seismograms are noisy, comparatively little energy traveling at the S wavespeed is observed, which favors the model of the second-order moment tensor.

The preferred secondary source components for shot 2 physically represent the uplift of a cylindrical volume of material directly above the explosion relative to the surrounding rock. The precise distribution of the additional inferred shear dislocations cannot be resolved, but the proposed mechanism is similar to that of the damage of an inverted conical region above the explosion proposed by Mosse (1981), that is, block motion accommodated by near-vertical shear along the walls of the conical region. Our model could be refined by a quantitative consideration of the vertical shear stress generated by the explosive source in order to localize those planes likely to undergo secondary shear failure. A more detailed model has been proposed by Sammis (2002) in which crack growth around the fault weakens the surrounding rock by decreasing its shear modulus, and secondary cracking according to his micromechanical model leads to additional source components. A nondimensional interpretation of our results suggests that the second-order moment-tensor source components scale with first-order moment-tensor components with the ratio ~0.4 times the depth of burial of the explosion.

The implosive components inferred for shots 3 and 5 represent the collapse of a void temporarily created by the explosion. Its moment M_{impl} relative to the explosion moment M_{expl} is likely related to the amount of local rock failure induced by the explosion. In the absence of rock damage or fracturing, the explosion should not produce a permanent volume change; that is, an implosion of net moment equal and opposite to the explosion is expected to follow the explosion. The fact that the ratio $M_{\text{impl}}/M_{\text{expl}}$ is only a fraction of unity (values of 0.34 and 0.43 for shots 3 and 5, respec-

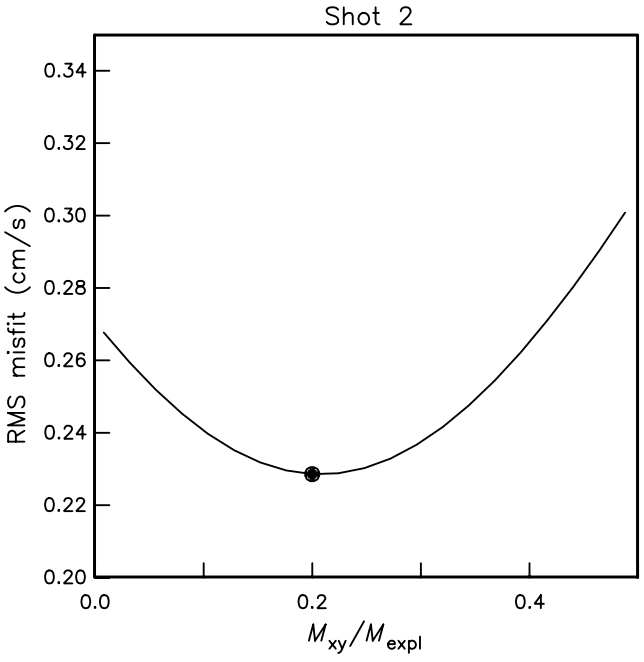

Figure 12. Root-mean-square misfit between observed and synthetic seismograms for shot 2 computed using 0.15 s-long portions of the contributing seismograms beginning just before the P arrival. The synthetics are calculated using the M_{expl} and M_{xy} source terms of equation (2). Optimal $M_{xy} = 0.20 \times M_{\text{expl}}$ is indicated with the solid circle.

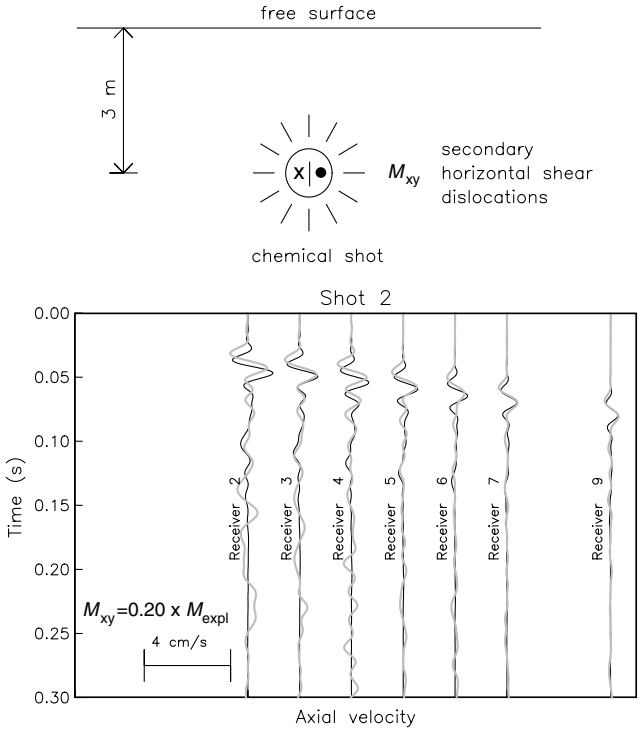

Figure 13. Observed axial-component seismograms (gray) and synthetic seismograms (black) for receivers 2–7 and 9, and recording shot 2 (Table 1). Synthetics are calculated using a combined explosion source and an additional moment tensor M_{xy} component with horizontal shear (equation 2). The inset indicates the geometry of the moment-tensor density, placed at the same location as the explosion source, used to represent the secondary shear dislocation. Other details are as in Figure 3.

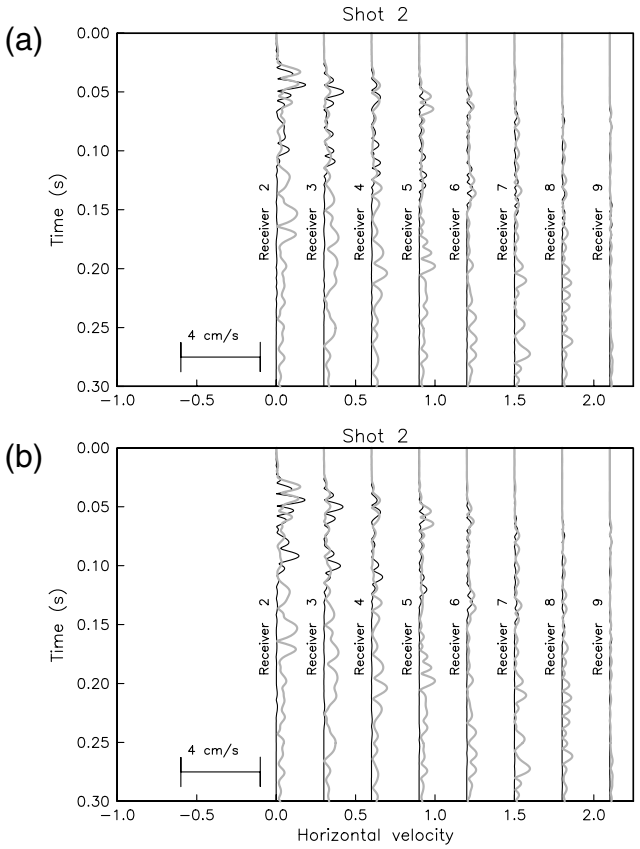

Figure 14. Amplitude of observed horizontal-component seismograms (gray) and synthetic seismograms (black) for receivers 2–7 and 9, and recording shot 2 (Table 1). (a) Synthetics are calculated using the combined explosion source and higher-order moment-tensor model (see the Nonexplosive Source Components section). (b) Synthetics are calculated using a combined explosion source and an additional moment tensor M_{xy} component with horizontal shear (equation 2). Other details are as in Figures 8 and 13.

tively) suggests a permanent macroscopic positive volume change and is in agreement with the positive static moment inferred by Patton *et al.* (2005) for a series of chemical shots (1997 Kazakhstan depth-of-burial experiment) of much greater yield and depth of burial than those studied here. The lack of a similar implosive component inferred for shot 2 may be attributed to the inferred upheaval of the cylindrical region above the shot, which accommodated to a large extent the volume change imparted by the explosion.

Conclusions

Downhole recordings of near-surface chemical explosions near the SAFOD main hole richly document the seismic wave field at distances of ~70–2300 m from the source. Waveform modeling of these shots reveals that, for smaller explosions, the effective source may be described, to first order, as the superposition of an explosive point source and secondary sources representing a distribution of vertical shear dislocations. For larger explosions, an additional implosive component, slightly delayed from the initial explosive source, is required. The nature of the secondary source components is likely more complicated than what is presented here, but our modeling suggests that they accommodate failure of a weak upper crustal rock in response to large local shear and isotropic stresses imparted by the chemical explosion.

Data and Resources

Seismic waveform data from the SAFOD main hole have been provided by Paulsson Geophysical Services, Inc.

Acknowledgments

We thank Coyn Criley of the U.S. Geological Survey (USGS) for conducting the shots. San Andreas Fault Observatory at Depth (SAFOD) is a part of Earthscope, a program funded by the National Science Foundation and carried out in cooperation with the USGS, the International Continental Scientific Drilling Program, Stanford University, and other agencies. We also thank Joe Fletcher and Paul Spudich for their comments on a preliminary draft as well as the Associate Editor and two anonymous reviewers for their constructive comments, which helped to improve this paper. This work has been partially supported by the National Nuclear Security Administration Award Number DE-AI52-09NA29328.

References

Aki, K., and P. G. Richards (1980). *Quantitative Seismology*, Vol. **1**, W. H. Freeman, San Francisco, 557 pp.

Backus, G., and M. Mulcahy (1976). Moment tensors and other phenomenological descriptions of seismic source, I. Continuous displacements, *Geophys. J. Roy. Astron. Soc.* **46,** 341–361.

Bouchon, M. (1981). A simple method to calculate Green's functions for elastic layered media, *Bull. Seismol. Soc. Am.* **71,** 959–971.

Brocher, T. M. (2005). Empirical relations between elastic wavespeeds and density in the Earth's crust, *Bull. Seismol. Soc. Am.* **95,** 2081–2092.

Chavarria, J. A., A. Goertz, M. Karrenbach, B. Paulsson, P. Milligan, V. Soutyrine, A. Hardin, D. Dushman, and L. LaFlame (2007). The use of VSP techniques for fault zone characterization: An example from the San Andreas fault, *The Leading Edge* **26,** 770–776.

Chavarria, J. A., P. Malin, R. Catchings, and E. Shalev (2003). A look inside the San Andreas fault at Parkfield through vertical seismic profiling, *Science* **302,** no. 5651, 1746–1748.

Dreger, D., and B. Woods (2002). Regional distance seismic moment tensors of nuclear explosions, *Tectonophysics* **356,** 139–156.

Friederich, W., and J. Dalkolmo (1995). Complete synthetic seismograms for a spherically symmetric earth by a numerical computation of the Green's function in the frequency domain, *Geophys. J. Int.* **122,** 537–550.

Gardner, G. H. F., L. W. Gardner, and A. R. Gregory (1974). Formation velocity and density—The diagnostic basics for stratigraphic traps, *Geophysics* **39,** 770–780.

Kuhn, M. J. (1985). A numerical study of Lamb's problem, *Geophys. Prospect.* **33,** 1103–1137.

McPhee, D., R. C. Jachens, and C. M. Wentworth (2004). Crustal structure across the San Andreas fault at the SAFOD site from potential field and geologic studies, *Geophys. Res. Lett.* **31,** L12S03.

Mosse, R. P. (1981). Review of seismic source models for underground nuclear explosions, *Bull. Seismol. Soc. Am.* **71,** 1249–1268.

Patton, H., and S. Taylor (1995). Analysis of *Lg* spectral ratios from NTS explosions: Implications for the source mechanisms of spall and the generation of *Lg* waves, *Bull. Seismol. Soc. Am.* **85,** 220–236.

Patton, H., and S. Taylor (2011). The apparent explosion moment: Inferences of volumetric moment due to source medium damage by underground nuclear explosions, *J. Geophys. Res.* **116,** B03310.

Patton, H., J. L. Bonner, and I. N. Gupta (2005). *Rg* excitation by underground explosions: Insights from source modelling the 1997 Kazakhstan depth-of-burial experiment, *Geophys. J. Int.* **163,** 1006–1024.

Press, F., and C. Archambeau (1962). Release of tectonic strain by underground nuclear explosions, *J. Geophys. Res.* **67,** 337–343.

Rubinstein, J. L., F. F. Pollitz, and W. L. Ellsworth (2011). Analysis and modeling of the wavefield generated by explosions at the San Andreas Fault Observatory at Depth, *Seismol. Res. Lett.* **82,** p. 272.

Sammis, C. G. (2002). Generation of high-frequency *P* and *S* wave energy by rock fracture during a buried explosion: Its effect on P/S discriminants at low magnitude, in *Proc. of the 2010 Monitoring Research Review: Ground-Based Nuclear Explosion Monitoring Technologies* Vol. I, Ponte Vedra Beach, Florida, 542–551, LA-UR-02-5048.

Stevens, J. L., T. G. Barker, S. M. Day, K. L. McLaughlin, N. Rimer, and B. Shkoller (1991). Simulation of teleseismic body waves, regional seismograms, and Rayleigh wave phase shifts using two-dimensional nonlinear models of explosion sources, in *Explosion Source Phenomenology*, S. Taylor, H. Patton, and P. Richards (Editors), American Geophysical Monograph **65**, 239–252.

Toksöz, M. M., D. G. Harkrider, and A. Ben-Menahem (1965). Determination of source parameters by amplitude equalization of seismic surface waves: Part 2, Release of tectonic strain by underground nuclear explosions and mechanisms of earthquakes, *J. Geophys. Res.* **70,** 907–922.

Woods, B. B., and D. V. Helmberger (1997). Regional seismic discriminants using wave-train energy ratios, *Bull. Seismol. Soc. Am.* **87,** 589–605.

Zhang, H., C. Thurber, and P. Bedrosian (2009). Joint inversion for Vp, Vs, and Vp/Vs at SAFOD, Parkfield, California, *Geochem. Geophys. Geosys.* **10,** Q11002, doi 10.1029/2009GC002709.

Zhu, L., and L. A. Rivera (2002). A note on the dynamic and static displacements from a point source in multilayered media, *Geophys. J. Int.* **148,** 619–627.

Zoback, M. D., S. Hickman, and W. Ellsworth (2010). Scientific drilling into the San Andreas fault zone, *Eos Trans. AGU* **91,** no. 22, 197–199.

U.S. Geological Survey
345 Middlefield Rd.
MS 977
Menlo Park, California 94025

Manuscript received 15 July 2011